

Probabilistic NDVI Forecasting from Sparse Satellite Time Series and Weather Covariates

Irene Iele^{*§}, Giulia Romoli^{†§}, Daniele Molino^{*}, Elena Mulero Ayllón^{*}, Filippo Ruffini^{*†},
Paolo Soda^{*†}, Matteo Tortora[‡]

^{*} Unit of Artificial Intelligence and Computer Systems, Università Campus Bio-Medico di Roma, Italy

[†] Department of Diagnostics and Intervention, Biomedical Engineering and Radiation Physics, Umeå University, Sweden

[‡] Department of Naval, Electrical, Electronics and Telecommunications Engineering, University of Genoa, Italy

Email: matteo.tortora@unige.it

[§]These authors contributed equally.

Abstract—Accurate short-term forecasting of vegetation dynamics is a key enabler for data-driven decision support in precision agriculture. Normalized Difference Vegetation Index (NDVI) forecasting from satellite observations, however, remains challenging due to sparse and irregular sampling caused by cloud coverage, as well as the heterogeneous climatic conditions under which crops evolve. In this work, we propose a probabilistic forecasting framework specifically designed for field-level NDVI prediction under clear-sky acquisition constraints. The method leverages a transformer-based architecture that explicitly separates the modeling of historical vegetation dynamics from future exogenous information, integrating historical NDVI observations with both historical and future meteorological covariates. To address irregular revisit patterns and horizon-dependent uncertainty, we introduce a temporal-distance weighted quantile loss that aligns the training objective with the effective forecasting horizon. In addition, we incorporate cumulative and extreme-weather feature engineering to better capture delayed meteorological effects relevant to vegetation response. Extensive experiments on European satellite data demonstrate that the proposed approach consistently outperforms a diverse set of statistical, deep learning, and recent time series baselines across both point-wise and probabilistic evaluation metrics. Ablation studies further highlight the central role of target history, while showing that meteorological covariates provide complementary gains when jointly exploited. The code is available at <https://github.com/arco-group/ndvi-forecasting>.

Index Terms—NDVI Forecasting, Multimodal Fusion, Irregular Sampling, Quantile Forecasting, Remote Sensing, Weather Covariates

I. INTRODUCTION

Precision agriculture aims to improve the efficiency and sustainability of farming practices by enabling timely, data-driven interventions that are tailored to local conditions. Farmers routinely face decisions on irrigation scheduling, fertilization, and stress mitigation, where short-term forecasts can reduce uncertainty and support proactive planning. In this context, Artificial Intelligence (AI) has become a key enabling technology across multiple stages of the agricultural production chain [1]–[4], fostering a shift from uniform management to more adaptive and data-informed strategies [5].

Satellite remote sensing provides scalable, non-invasive monitoring of crop dynamics over large areas and repeated time intervals, complementing in-field sensing solutions that may be unavailable or difficult to deploy at scale [6], [7]. Multispectral observations enable the computation of Vegetation Indices (VIs) that capture vegetation properties related to phenology and stress response [8], [9]. Among them, the Normalized Difference Vegetation Index (NDVI) is widely used as a proxy for vegetation greenness and canopy development, offering a practical signal for monitoring and forecasting vegetation condition.

Despite improvements in spatial, spectral, and temporal resolution, operational NDVI forecasting remains challenging. In particular, clear-sky Sentinel-2 observations yield time series that are sparse and irregular due to revisit patterns and cloud masking. Moreover, forecasting performance can degrade under heterogeneous climatic and environmental conditions, limiting generalization across regions and growing seasons [10], [11]. These factors motivate learning approaches that explicitly account for irregular sampling and leverage complementary information sources, such as meteorological covariates. More generally, combining heterogeneous yet complementary sources can improve robustness in real-world prediction tasks, motivating multimodal learning strategies [12].

VI forecasting can be formulated at different output granularities. A first line of work targets field-level trajectories, where VIs are aggregated over parcels or regions and modeled as time series. A second line of work addresses pixel-level forecasting and aims to generate dense maps of future vegetation states from spatio-temporal image inputs. This paper focuses on field-level NDVI forecasting under sparse and irregular clear-sky observations, which is directly aligned with short-term decision support. Field-level NDVI forecasting has been widely studied using deep learning models trained on VI sequences and auxiliary variables [13]–[16]. Recurrent architectures are particularly common, including ConvLSTM models with meteorological covariates [17], [18], graph-based extensions to capture spatial dependencies [19], and alignment-based formulations to disentangle seasonal and short-term dynamics [20]. More recent studies highlight the importance of robustness across heterogeneous European cli-

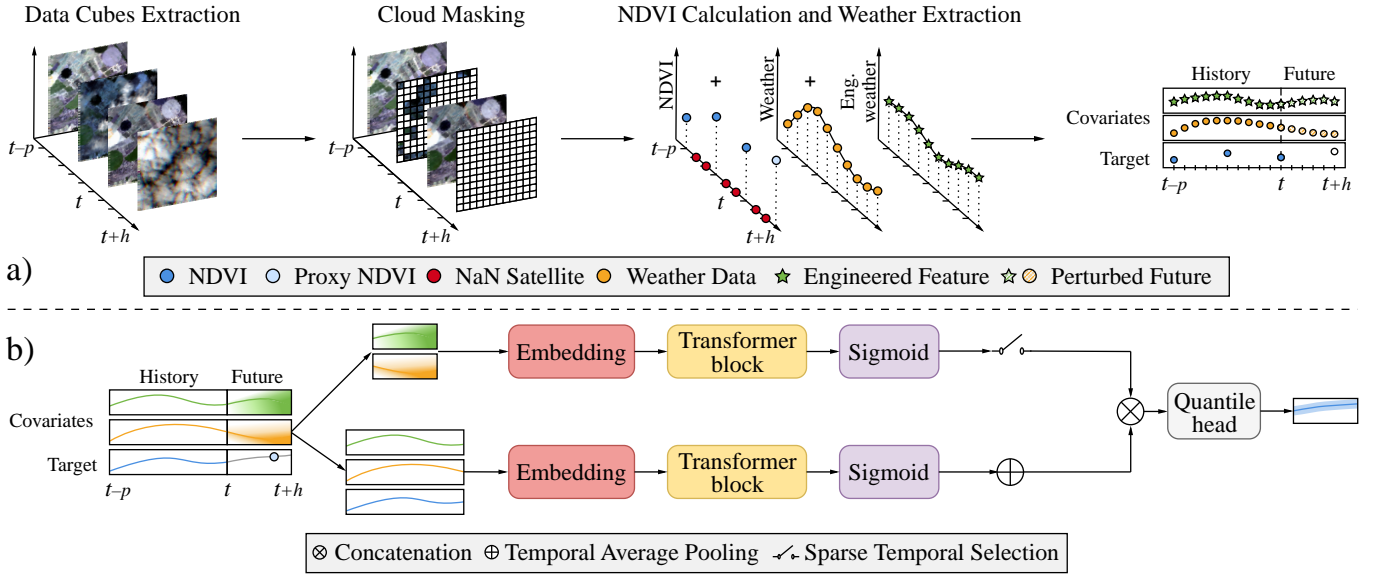


Fig. 1. Overview of the proposed pipeline for probabilistic NDVI forecasting. (a) Sentinel-2 cubes are cloud-masked to derive clear-sky NDVI, combined with meteorological series and engineered features; future covariates are perturbed to model forecast uncertainty. (b) Transformer-based probabilistic forecasting architecture with decoupled history and future branches. Historical observations are encoded through a dedicated transformer encoder and aggregated via temporal average pooling. Future meteorological covariates are processed by a separate transformer encoder; due to irregular satellite revisit times, sparse temporal selection retains only embeddings corresponding to actual Sentinel-2 acquisition dates. The pooled history representation is concatenated with the selected future embeddings and passed to a quantile prediction head, which outputs multi-step NDVI quantiles at $q \in \{0.1, 0.5, 0.9\}$, providing both point forecasts and calibrated uncertainty estimates.

mates [21], while often relying on regularized or densified time series. Overall, existing studies often rely on regular composites or implicitly densify the signal, while robustness under sparse and irregular clear-sky acquisitions remains less explored. Pixel-level approaches address a different objective by forecasting full-resolution VI maps. ContextFormer [22] is a multimodal spatio-temporal transformer trained to predict NDVI at high spatial resolution using cloud-masked Sentinel-2 imagery and auxiliary geospatial variables. VegeDiff [23] further introduces a diffusion-based probabilistic framework to model multiple plausible futures and extends predictions beyond NDVI. While these methods provide detailed spatial forecasts, they require dense spatial inputs and outputs and are evaluated under image forecasting criteria, which are not directly comparable to field-level trajectory prediction under sparse clear-sky sampling.

This work introduces a probabilistic forecasting framework designed to generalize across diverse European ecozones and growing seasons. We employ a self-attention transformer that integrates historical NDVI with historical and future weather covariates to predict NDVI quantiles up to 14 days ahead. The proposed design explicitly addresses sparse and irregular clear-sky sampling and supports short-term decision support.

The main contributions are summarized as follows:

- We address field-level NDVI forecasting under sparse and irregular clear-sky satellite observations by proposing a transformer-based quantile model that jointly exploits historical NDVI, historical weather, and future weather covariates for probabilistic multi-step prediction.

- We introduce a temporal-distance weighted quantile loss to better handle variable forecasting horizons induced by irregular revisit patterns.
- We propose a weather feature engineering strategy that captures cumulative and extreme conditions over variable-length intervals, improving the alignment between daily meteorology and irregular NDVI observations.
- We validate the approach across multiple European ecozones and growing seasons against statistical, deep learning, and recent time series baselines, and quantify the impact of each component via ablation studies.

Code and pre-trained models will be made publicly available through an online repository.

II. MATERIALS

In this study, we use the GreenEarthNet dataset [22], which provides spatio-temporal data cubes coupling cloud-masked Sentinel-2 image sequences with meteorological time series. The dataset includes 24,861 data cubes over Europe from 2017 to 2022; each cube includes 30 cloud-masked Sentinel-2 images at 5-day intervals (128×128 pixels spanning 2.56×2.56 km) and 150 daily meteorological observations¹. Following the official dataset split, we use the train subset, covering the period 2017–2019, for model training, and the validation subset, corresponding to year 2020, for validation.

¹Wind speed, relative humidity, shortwave down-welling radiation, rainfall, sea-level pressure, and temperature.

The Sentinel-2 images include blue (B02), green (B03), red (B04), and near infrared (B8A) bands at a spatial resolution of 20m, from which NDVI is computed as:

$$\text{NDVI} = \frac{\text{B8A} - \text{B04}}{\text{B8A} + \text{B04}} \quad (1)$$

A pre-processing pipeline has been implemented to enrich the data cubes with climate information and extract NDVI time series from the cube images, as illustrated in Figure 1 (panel a). We then developed a procedure to extract temporal NDVI series from the data cubes. For each cube, pixels are selected from each satellite image based on cloud coverage. NDVI is then calculated by averaging the values of the selected pixels for each time step, generating a temporal NDVI series to be analyzed together with the meteorological time series. This choice prioritizes the physical reliability of the vegetation signal, at the cost of an irregular temporal sampling induced by cloud masking.

Formally, we consider a supervised time series forecasting problem. Let $\{(y_t, \tau_t, x_t)\}_{t=1}^T$ denote the dataset, where $y_t \in \mathbb{R}$ is the reconstructed clear-sky NDVI target associated with the t -th target observation, τ_t is its real acquisition time, and $x_t \in \mathbb{R}^d$ collects the corresponding exogenous covariates. Given a reference index t , the model receives the target history $\mathbf{y}_{t-p:t-1} = (y_{t-p}, \dots, y_{t-1})$, the historical covariates $\mathbf{x}_{t-p:t-1} = (x_{t-p}, \dots, x_{t-1})$, and the future exogenous covariates $\mathbf{x}_{t:t+h} = (x_t, \dots, x_{t+h})$, and predicts the future target sequence $\hat{\mathbf{y}}_{t:t+h} = (\hat{y}_t, \dots, \hat{y}_{t+h})$. Here, p denotes the history length and h the forecasting horizon. Since indices t refer to ordered target observations rather than fixed temporal steps, the real-time spacing between consecutive targets $\tau_{t+1} - \tau_t$ is generally irregular. Consequently, the effective forecasting horizon spans $\tau_{t+h} - \tau_t$ and may vary across samples depending on the Sentinel-2 acquisition schedule. Because clear-sky observations are not always available at every satellite overpass, the resulting NDVI time series contains missing values at several acquisition dates. This occurs when a Sentinel-2 acquisition is fully affected by cloud coverage, resulting in the absence of any reliable NDVI measurement at that timestamp. To enable consistent temporal modeling, the clear-sky NDVI signal is therefore reconstructed through temporal interpolation. Interpolation explicitly accounts for the actual temporal distance between consecutive satellite acquisitions, ensuring that the reconstructed signal remains aligned with the true observation timeline and does not introduce artificial temporal patterns. Importantly, interpolation is applied exclusively at timestamps corresponding to existing satellite acquisitions for which the vegetation signal is entirely obscured by clouds, and not at timestamps where no ground-truth acquisition is available. Specifically, given two consecutive clear-sky observations (τ_0, y_0) and (τ_1, y_1) , the NDVI value at an intermediate acquisition timestamp $\tau \in (\tau_0, \tau_1)$ is obtained via time-aware linear interpolation as

$$y(\tau) = y_0 + \frac{\tau - \tau_0}{\tau_1 - \tau_0} (y_1 - y_0). \quad (2)$$

From the reconstructed series, forecasting samples are generated using a sliding-window strategy defined in the observation space rather than in continuous time. Specifically, windows are constructed over the sequence of available NDVI target values (observed or reconstructed), which occur only at Sentinel-2 satellite overpass timestamps. As a result, the target time series is sparse and irregularly sampled in time, since no target values are available between consecutive satellite acquisitions. The history and forecasting horizons are set to $p = 3$ and $h = 3$, respectively, with a shift of four target observations, corresponding to a short-term predictive horizon of approximately 14 days depending on the satellite revisit schedule. This temporal range is commonly regarded as appropriate for operational decision support in agriculture, as it enables timely planning of irrigation, fertilization, and crop management interventions while limiting uncertainty accumulation [18], [24]. Temporal information is encoded using cyclical representations of the day of the year to capture seasonal dynamics. A Fourier-based encoding is adopted, in which sine and cosine components are computed for multiple harmonics up to order three. Formally, for a given day of the year d , the cyclical encoding is defined as

$$\left\{ \sin\left(2\pi s \frac{d-1}{366}\right), \cos\left(2\pi s \frac{d-1}{366}\right) \right\}_{s=1}^3. \quad (3)$$

Here, s denotes the harmonic index of the Fourier-based cyclical encoding, with a maximum value of 3. This choice provides a balance between expressive power and robustness, allowing the model to capture sub-seasonal patterns while avoiding high-frequency components that could amplify noise. Meteorological variables are incorporated as exogenous covariates and further enriched through cumulative feature engineering to capture delayed and extreme weather effects relevant to vegetation dynamics. Specifically, nine derived features are computed from precipitation and temperature using two complementary aggregation strategies.

a) Between-target cumulative features: To account for the irregular spacing of target observations, three features are computed by aggregating daily meteorological variables over the variable-length interval between two consecutive target timestamps τ_{t-1} and τ_t . These features capture cumulative effects occurring between successive satellite overpasses and are defined as

$$\text{Rain}_t^{\text{bt}} = \sum_{\tau \in (\tau_{t-1}, \tau_t]} r(\tau), \quad (4)$$

$$\text{Cold}_t^{\text{bt}} = \sum_{\tau \in (\tau_{t-1}, \tau_t]} \mathbb{I}(T(\tau) < 10^\circ\text{C}), \quad (5)$$

$$\text{Hot}_t^{\text{bt}} = \sum_{\tau \in (\tau_{t-1}, \tau_t]} \mathbb{I}(T(\tau) > 30^\circ\text{C}), \quad (6)$$

corresponding respectively to cumulative rainfall, the number of cold days, and the number of hot days observed between two consecutive target acquisitions.

b) Rolling-window cumulative features: In addition, six features are computed using rolling aggregation over fixed tem-

poral windows to capture short- and medium-term weather effects independently of the target sampling irregularity. Let $w \in \{7, 14\}$ denote the rolling window length (in days), and let

$$W_w(\tau_t) = (\tau_t - w, \tau_t] \quad (7)$$

be the set of daily timestamps within the window ending at target time τ_t . The rolling cumulative features are defined as

$$\text{Rain}_{t,w}^{\text{roll}} = \sum_{\tau \in W_w(\tau_t)} r(\tau), \quad (8)$$

$$\text{Cold}_{t,w}^{\text{roll}} = \sum_{\tau \in W_w(\tau_t)} \mathbb{I}(T(\tau) < 10^\circ\text{C}), \quad (9)$$

$$\text{Hot}_{t,w}^{\text{roll}} = \sum_{\tau \in W_w(\tau_t)} \mathbb{I}(T(\tau) > 30^\circ\text{C}), \quad (10)$$

which correspond to cumulative rainfall and counts of extreme-temperature days over fixed temporal horizons. The temperature thresholds of 10°C and 30°C are commonly adopted in agronomic studies as indicators of cold and heat stress conditions affecting plant physiology and, in extreme cases, leading to growth inhibition or tissue damage [24]. The same set of cumulative features is computed for both historical and future covariates.

To account for uncertainty in meteorological forecasts, controlled perturbations are applied to future meteorological covariates. The magnitude of the perturbation increases with the temporal distance from the last observed historical timestamp, reflecting the growing uncertainty at longer forecasting horizons. This is implemented through a horizon-dependent scaling factor

$$g_k = 1 + \beta \cdot \Delta t_k, \quad (11)$$

where Δt_k denotes the temporal distance (in days) between the k -th future timestamp and the last historical observation. β is chosen such that the scaling factor at the last future step satisfies $g_K = 2$, meaning that the noise magnitude at the furthest horizon is twice the base level. Overall, the perturbation corresponds to a noise level of 10% of the variable magnitude and is applied multiplicatively to the future meteorological covariates, with the scaling factor g_k modulating the perturbation strength as a function of the forecasting horizon. Finally, following [25], all variables are normalized using a robust scaling strategy computed globally on the training data. For a generic variable x , normalization is defined as

$$x' = \text{arcsinh} \left(\frac{x - \mu}{\sqrt{\sigma^2 + \varepsilon}} \right), \quad (12)$$

where μ and σ^2 denote the mean and variance estimated on the training set and ε is a small constant for numerical stability.

III. METHODS

The proposed architecture, depicted in Figure 1 (panel b), is designed for quantile-based time series forecasting and explicitly separates the modeling of historical observations from that of future exogenous covariates. The overall transformer-based design is inspired by [26], from which we adopt the

use of independent encoder branches to process historical and future information, while introducing several task-specific modifications.

The history encoder processes the past target sequence together with the corresponding historical covariates, while the future encoder processes the sequence of known future covariates. Each input sequence is first projected through a linear embedding layer into a shared latent space of dimension d_{model} , allowing heterogeneous features to be represented in a common space. Positional information is then injected via positional encoding to preserve the temporal ordering of observations within each sequence. Missing values, arising from sparse and irregular acquisitions are explicitly handled through binary masking in both historical and future branches. Specifically, masks mark target positions with no corresponding Sentinel-2 acquisitions (i.e. unobserved NDVI targets between consecutive overpasses). These masks are propagated through the self-attention layers of each transformer encoder to prevent the model from attending to missing tokens.

The output of the history encoder is aggregated via *temporal average pooling* to obtain a compact representation of the past context. In contrast, due to the sparse and irregular satellite revisit schedule, the output of the future encoder is processed through a *sparse temporal selection* mechanism, retaining only embeddings corresponding to actual satellite acquisition times. Specifically, the future encoder processes the full sequence of future covariates through self-attention, allowing information from all intermediate timesteps to influence the learned representations. From this encoded sequence, only the embeddings corresponding to Sentinel-2 acquisition times are selected for prediction. The pooled history representation is then concatenated with the selected future embeddings along the feature dimension, yielding a joint representation that conditions each future prediction on both past observations and future exogenous information.

This fused representation is propagated through a quantile head that predicts, for each future timestep, a vector of quantile estimates. Specifically, the model predicts three quantiles, corresponding to $q \in \{0.1, 0.5, 0.9\}$ levels. The median quantile ($q = 0.5$) is treated as the primary point forecast of the model, while the lower and upper quantiles provide an explicit characterization of predictive uncertainty. All future timesteps are predicted in parallel, without autoregressive decoding.

The model is trained using the quantile pinball loss, which for a quantile level $q_i \in (0, 1)$ is defined as:

$$\mathcal{L}_{q_i} = |y_i - \hat{y}_{i,q_i}| \left(q_i \cdot \mathbb{I}(y_i - \hat{y}_{i,q_i} \geq 0) + (1 - q_i) \cdot \mathbb{I}(y_i - \hat{y}_{i,q_i} < 0) \right). \quad (13)$$

Here, y_i is the ground-truth target, \hat{y}_{i,q_i} is the predicted quantile at level q_i , and $\mathbb{I}(\cdot)$ denotes the indicator function. To account for the irregular temporal spacing between target observations and the increasing uncertainty at longer forecasting horizons, the loss contribution of each future target is weighted according to its temporal distance from the last available historical observation. For a future target occurring

TABLE I
CLEAR-SKY NDVI FORECASTING RESULTS (MEAN \pm STD) FOR THE PROPOSED MODEL AND BASELINES. THE PROPOSED MODEL IS HIGHLIGHTED IN BLUE. **BOLD** VALUES DENOTE THE BEST RESULTS.

Architecture	RMSE \downarrow	MAE \downarrow	WMAPE \downarrow	MASE \downarrow	CRPS \downarrow	Pinball \downarrow
AutoARIMA	0.1442 \pm 0.2172	0.0926 \pm 0.1105	0.1959 \pm 0.2338	1.0715 \pm 1.2783	0.0617 \pm 0.0771	0.1080 \pm 0.0408
LSTMPlus	0.1149 \pm 0.1479	0.0812 \pm 0.0812	0.1677 \pm 0.1677	1.4583 \pm 1.4580	0.0515 \pm 0.0583	0.0881 \pm 0.0222
RNNPlus	0.1064 \pm 0.1414	0.0758 \pm 0.0747	0.1565 \pm 0.1541	1.3608 \pm 1.3401	0.0526 \pm 0.0569	0.0936 \pm 0.0070
DeepAR	0.0941 \pm 0.1504	0.0606 \pm 0.0721	0.1250 \pm 0.1488	1.0869 \pm 1.2937	0.0389 \pm 0.0523	0.0669 \pm 0.0381
InceptionTimePlus	0.1033 \pm 0.1428	0.0725 \pm 0.0735	0.1497 \pm 0.1518	1.3017 \pm 1.3201	0.0526 \pm 0.0576	0.0952 \pm 0.0168
PatchTST	0.0987 \pm 0.1433	0.0668 \pm 0.0726	0.1379 \pm 0.1499	1.1988 \pm 1.3039	0.0405 \pm 0.0468	0.0677 \pm 0.0149
TimeLLM	0.0903 \pm 0.1557	0.0565 \pm 0.0704	0.1168 \pm 0.1453	1.0158 \pm 1.2640	–	–
Ours	0.0821\pm0.1605	0.0509\pm0.0644	0.1051\pm0.1331	0.9146\pm1.1576	0.0315\pm0.0448	0.0177\pm0.0268

at timestamp τ_{t+k} , this distance is defined as

$$\Delta\text{days}_k = \tau_{t+k} - \tau_{t-1}, \quad (14)$$

expressed in days. A corresponding horizon-dependent weight is then assigned as

$$w_k = \frac{1}{1 + \alpha \cdot \Delta\text{days}_k}, \quad (15)$$

where $\alpha = 0.5$ is a scaling parameter controlling the rate of decay. This weighting strategy stabilizes training and reflects the increasing intrinsic uncertainty of longer-term forecasts.

IV. EXPERIMENTAL CONFIGURATION

A. Evaluation metrics

We report standard point-forecast errors (RMSE, MAE, WMAPE, and MASE) [26] computed on the median prediction ($q = 0.5$). For probabilistic assessment, we use the Continuous Ranked Probability Score (CRPS), which compares the predicted CDF $F(\cdot)$ with the observation y :

$$\text{CRPS}(F, y) = \int_{-\infty}^{+\infty} (F(z) - \mathbb{I}(z \geq y))^2 dz. \quad (16)$$

Lower values indicate better performance for all metrics.

B. Competitors

We evaluate the proposed approach against a diverse set of forecasting baselines, each representing a different modeling paradigm. As a classical statistical baseline, we include AutoARIMA [27], which relies on automated ARIMA model selection for time series forecasting. Recurrent approaches are represented by LSTMPlus [28] and RNNPlus [29], which model temporal dynamics through sequential hidden-state updates, as well as DeepAR [30], a probabilistic autoregressive model that estimates the conditional distribution of future values and provides uncertainty-aware forecasts. As a convolutional baseline, we consider InceptionTimePlus [31], which employs parallel convolutional kernels of different lengths to capture temporal patterns at multiple resolutions. Transformer-based methods are represented by PatchTST [32], which segments input time series into overlapping patches and applies a channel-independent transformer encoder to efficiently capture both local and long-range temporal dependencies. Finally,

TimeLLM [33] adopts a large language model formulation that reformulates time series forecasting as a language modeling task through suitable input reprogramming. RNNPlus, LSTMPlus, InceptionTimePlus, and PatchTST are implemented using the tsai library [34], DeepAR and AutoARIMA are evaluated using the AutoGluon framework [35], while TimeLLM is implemented using the NeuralForecast library [36]. All baselines operate in the multivariate setting, exploiting both target history and covariate information, except for TimeLLM and AutoARIMA, as they do not support multivariate inputs or exogenous covariates and therefore rely solely on the target history.

C. Implementation details

The model is implemented in PyTorch and optimized with Adam for 200 epochs (batch size 128, initial learning rate 10^{-4}). A validation-driven scheduler reduces the learning rate by a factor of 0.2 after 20 epochs without improvement, down to 5×10^{-5} . Both the history and future branches use identical transformer encoders with 8 layers, $d_{\text{model}} = 128$, 8 attention heads, and a 512-dimensional feed-forward network. Dropout ($p = 0.1$) is applied throughout the transformer blocks. All experiments are conducted on a workstation equipped with an NVIDIA T4 GPU.

V. RESULTS

This section presents a comprehensive evaluation of the proposed NDVI forecasting framework. We first compare overall forecasting performance against established baselines, then conduct two ablation studies analyzing the effect of temporal loss weighting and feature engineering, as well as the contribution of target, historical, and future inputs, and finally present ground-truth versus predicted NDVI scatter plots across different climate regions.

A. Comparative analysis

Table I presents a comparative evaluation of forecasting performance on the clear-sky NDVI task across a diverse set of baseline models. All methods are evaluated under the same experimental protocol using the evaluation metrics introduced earlier, with results computed on the test set and lower values indicating better performance. It is worth noting that TimeLLM produces deterministic forecasts and therefore

TABLE II
ABLATION STUDY ON TEMPORAL LOSS WEIGHTING (w_k) AND METEOROLOGICAL FEATURE ENGINEERING (FT-ENG) FOR NDVI FORECASTING (MEAN \pm STD). \checkmark INDICATES PRESENCE AND \times ABSENCE.

w_k	ft-eng	RMSE \downarrow	MAE \downarrow	WMAPE \downarrow	MASE \downarrow	CRPS \downarrow	Pinball \downarrow
\times	\times	0.0834 \pm 0.1650	0.0514 \pm 0.0657	0.1062 \pm 0.1356	0.9234 \pm 1.1789	0.0318 \pm 0.0454	0.0179 \pm 0.0271
\times	\checkmark	0.0831 \pm 0.1607	0.0514 \pm 0.0654	0.1060 \pm 0.1349	0.9222 \pm 1.1733	0.0318 \pm 0.0448	0.0179 \pm 0.0266
\checkmark	\times	0.0827 \pm 0.1630	0.0512 \pm 0.0650	0.1057 \pm 0.1341	0.9190 \pm 1.1662	0.0318 \pm 0.0453	0.0180 \pm 0.0271
\checkmark	\checkmark	0.0821\pm0.1605	0.0509\pm0.0644	0.1051\pm0.1331	0.9146\pm1.1576	0.0315\pm0.0448	0.0177\pm0.0268

TABLE III
ABLATION STUDY ON CLEAR-SKY NDVI FORECASTING MODELS. EACH CONFIGURATION ENABLES (\checkmark) OR DISABLES (\times) CONDITIONING ON FUTURE METEOROLOGICAL COVARIATES (FUTURE), HISTORICAL METEOROLOGICAL COVARIATES (HISTORY), AND PAST TARGET VALUES (TARGET), AS WELL AS THEIR COMBINATIONS.

Future	History	Target	RMSE \downarrow	MAE \downarrow	WMAPE \downarrow	MASE \downarrow	CRPS \downarrow	Pinball \downarrow
\times	\checkmark	\checkmark	0.0871 \pm 0.1640	0.0543 \pm 0.0681	0.1122 \pm 0.1405	0.9756 \pm 1.2217	0.0338 \pm 0.0478	0.0191 \pm 0.0286
\checkmark	\checkmark	\times	0.1568 \pm 0.1348	0.1207 \pm 0.1001	0.2492 \pm 0.2066	2.1669 \pm 1.7969	0.0736 \pm 0.0673	0.0412 \pm 0.0397
\checkmark	\times	\checkmark	0.0858 \pm 0.1605	0.0532 \pm 0.0673	0.1098 \pm 0.1390	0.9547 \pm 1.2086	0.0332 \pm 0.0466	0.0188 \pm 0.0278
\times	\times	\checkmark	0.0855 \pm 0.1530	0.0523 \pm 0.0676	0.1080 \pm 0.1397	0.9388 \pm 1.2144	0.0320 \pm 0.0439	0.0180 \pm 0.0256
\times	\checkmark	\times	0.1643 \pm 0.1324	0.1284 \pm 0.1026	0.2650 \pm 0.2118	2.3048 \pm 1.8418	0.0771 \pm 0.0672	0.0429 \pm 0.0393
\checkmark	\times	\times	0.1849 \pm 0.1314	0.1495 \pm 0.1088	0.3086 \pm 0.2247	2.6833 \pm 1.9538	0.0929 \pm 0.0766	0.0525 \pm 0.0459
\checkmark	\checkmark	\checkmark	0.0821\pm0.1605	0.0509\pm0.0644	0.1051\pm0.1331	0.9146\pm1.1576	0.0315\pm0.0448	0.0177\pm0.0268

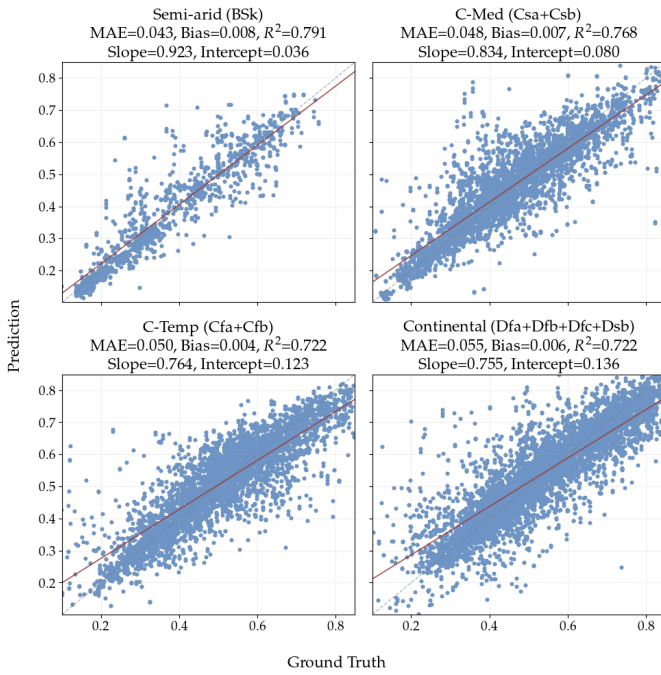


Fig. 2. Ground truth versus predicted NDVI by aggregated Köppen–Geiger climate group. The gray dashed line shows the 1:1 reference, and the red line shows the linear fit.

does not support probabilistic evaluation; as a result, CRPS and pinball loss are not reported for this model. Across all point-wise and probabilistic metrics, the proposed approach achieves the best results, as highlighted by the bold entries in the table. Statistical significance is assessed using the Diebold–Mariano test [37] with a Newey–West heteroskedasticity and autocorrelation consistent variance correction. The truncation

lag is set according to the three-step forecasting horizon. All pairwise comparisons yield p-values < 0.001 , confirming that the observed improvements are statistically significant.

B. Ablation study on temporal loss weighting and feature engineering

Table II evaluates the impact of temporal loss weighting (w_k) and engineered meteorological features (*ft-eng*). Disabling w_k corresponds to uniform weighting of future errors in the pinball loss. Both components improve performance across point-wise and probabilistic metrics. Temporal weighting provides the largest gains, consistent with accounting for irregular temporal spacing and horizon-dependent uncertainty. Feature engineering yields smaller but consistent improvements, indicating that cumulative and extreme-weather descriptors complement raw meteorological covariates. The best results, as highlighted by the bold entries in the table, are obtained when both components are enabled.

C. Ablation study on input modalities

Table III assesses the contribution of the input modalities on the clear-sky NDVI forecasting task, namely target history, historical meteorological covariates, and future meteorological covariates. Removing target history produces the largest degradation across both point-wise and probabilistic metrics, indicating that recent vegetation dynamics provide the dominant signal at short horizons. Historical meteorological covariates yield consistent secondary gains when combined with target history, improving both accuracy and uncertainty estimation. Future covariates alone are not sufficient to achieve competitive performance, but provide additional improvements when integrated jointly with target history and historical covariates. Overall, the ablation results suggest a clear hierarchy among modalities: target history is primary, historical covariates act

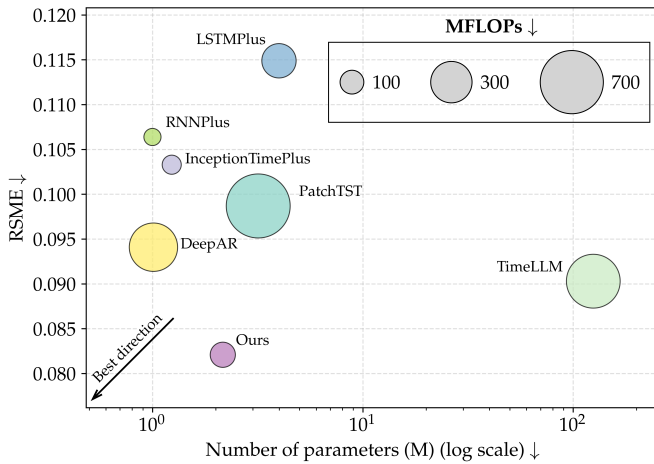


Fig. 3. Comparison of forecasting models in terms of RMSE (y-axis, lower is better) and parameter count in millions (x-axis, log scale; lower is better). Bubble size denotes inference cost (MFLOPs, batch size 1). The arrow highlights the desirable region (low RMSE with smaller models)

as supportive context, and future covariates contribute incremental gains in the full multimodal setting.

D. NDVI prediction across climate regions

To further assess the robustness of the proposed model under heterogeneous environmental conditions, Figure 2 reports ground truth versus predicted NDVI scatter plots stratified by aggregated Köppen–Geiger climate groups. Across all climates, predictions remain tightly aligned with the 1:1 line, indicating a consistent global mapping between inputs and targets. However, performance degrades from semi-arid to temperate/continental regimes: MAE increases from 0.043 in Semi-arid climates to 0.055 in Continental climates, while R^2 (fraction of explained variance) decreases from 0.791 to 0.722. The mean bias is consistently small and positive (0.004–0.008), suggesting a mild overestimation tendency that is secondary to the dominant error component, i.e., the increased dispersion around the diagonal. Notably, C-Med, C-temp and Continental climates exhibit a broader spread, especially at intermediate NDVI levels, consistent with higher phenological variability and observation noise (e.g., persistent cloud cover and seasonal effects), which jointly increase prediction uncertainty.

E. Computational analysis

Figure 3 compares models in terms of MFLOPs per forward pass (batch size 1) and trainable parameters. The proposed method requires 112.0 MFLOPs and 2.16 M parameters while achieving the lowest RMSE. Relative to PatchTST, our model reduces MFLOPs by approximately 85% while improving forecasting accuracy. Compared to InceptionTimePlus and recurrent baselines, the proposed architecture incurs a higher computational cost, reflecting the additional multimodal modelling capacity, but yields consistently lower errors. TimeLLM exhibits substantially higher model size and computational cost without corresponding performance gains. Overall, the

proposed approach provides a favorable accuracy-complexity trade-off for NDVI forecasting.

VI. CONCLUSION

This work presents a probabilistic framework for short-term NDVI forecasting from sparse and irregular clear-sky satellite time series, integrating historical vegetation dynamics with meteorological covariates through a transformer-based architecture. By explicitly separating the modeling of past observations and future exogenous information, and by accounting for temporal irregularity and horizon-dependent uncertainty, the proposed approach provides reliable multi-step NDVI forecasts together with calibrated uncertainty estimates. Experimental results on large-scale European data show consistent improvements over statistical, deep learning, and recent time series baselines across both point-wise and probabilistic metrics. Ablation studies confirm that target history is the primary driver of performance, while meteorological covariates provide complementary gains when jointly exploited. In addition, stratified analyses across climate groups indicate stable behavior under heterogeneous environmental conditions. This study has limitations. The evaluation is restricted to European agricultural areas, and generalization to other regions remains to be assessed, where crop phenology, management practices, and climate regimes may differ. Future work will extend the framework by incorporating explicit climate-zone and crop-type conditioning to improve climate-aware generalization and robustness in heterogeneous agricultural landscapes.

VII. ACKNOWLEDGMENTS

Irene Iele and Daniele Molino are Ph.D. students enrolled in the National Ph.D. in Artificial Intelligence, course on Health and Life Sciences, organized by Università Campus Bio-Medico di Roma. We acknowledge the EuroHPC Joint Undertaking for granting this project access to the EuroHPC supercomputer Vega, hosted by the Institute of Information Science (Slovenia), under a EuroHPC Development Access call.

REFERENCES

- [1] A. O. Adewusi *et al.*, “AI in precision agriculture: A review of technologies for sustainable farming practices,” *World Journal of Advanced Research and Reviews*, vol. 21, no. 1, pp. 2276–2285, 2024.
- [2] R. Upadhyay *et al.*, “Artificial intelligence in precision agriculture: A comprehensive review,” in *2024 7th International Conference on Contemporary Computing and Informatics (IC3I)*, vol. 7. IEEE, 2024, pp. 918–923.
- [3] N. Gangwani, “AI-driven precision agriculture: Optimizing crop yield and resource efficiency,” *Computer*, vol. 6, no. 1, 2024.
- [4] M. Tortora *et al.*, “Towards a Sustainable Future: AI-Powered Solutions in Agriculture and Green Energy,” 2025.
- [5] S. Misra *et al.*, “Agriculture paradigm shift: a journey from traditional to modern agriculture,” in *Biodiversity and bioeconomy*. Elsevier, 2024, pp. 113–141.
- [6] R. Zhang *et al.*, “Phenonet: A two-stage lightweight deep learning framework for real-time wheat phenophase classification,” *ISPRS Journal of Photogrammetry and Remote Sensing*, vol. 208, pp. 136–157, 2024.
- [7] P. Pal *et al.*, “Unmanned aerial system and machine learning driven digital-twin framework for in-season cotton growth forecasting,” *Computers and Electronics in Agriculture*, vol. 228, p. 109589, 2025.

- [8] J. Xue *et al.*, "Significant remote sensing vegetation indices: A review of developments and applications," *Journal of sensors*, vol. 2017, no. 1, p. 1353691, 2017.
- [9] Z. Gong *et al.*, "Satellite remote sensing of vegetation phenology: Progress, challenges, and opportunities," *ISPRS Journal of Photogrammetry and Remote Sensing*, vol. 217, pp. 149–164, 2024.
- [10] R. P. Sishodia *et al.*, "Applications of remote sensing in precision agriculture: A review," *Remote sensing*, vol. 12, no. 19, p. 3136, 2020.
- [11] W. A. Demissie *et al.*, "Integration of artificial intelligence and remote sensing for crop yield prediction and crop growth parameter estimation in mediterranean agroecosystems: Methodologies, emerging technologies, research gaps, and future directions," *European Journal of Agronomy*, vol. 173, p. 127894, 2026.
- [12] M. Tortora *et al.*, "Radiopathomics: multimodal learning in non-small cell lung cancer for adaptive radiotherapy," *IEEE Access*, vol. 11, pp. 47 563–47 578, 2023.
- [13] J. Olamofe *et al.*, "Normalized difference vegetation index prediction using reservoir computing and pretrained language models," *Artificial Intelligence in Agriculture*, vol. 15, no. 1, pp. 116–129, 2025.
- [14] N. Shamloo *et al.*, "An integrated artificial intelligence-deep learning approach for vegetation canopy assessment and monitoring through satellite images," *Stochastic Environmental Research and Risk Assessment*, pp. 1–23, 2025.
- [15] A. Marsetič *et al.*, "Forecasting vegetation behavior based on planetscope time series data using rnn-based models," *IEEE Journal of Selected Topics in Applied Earth Observations and Remote Sensing*, vol. 17, pp. 5015–5025, 2024.
- [16] A. Ferchichi *et al.*, "Multi-attention generative adversarial network for multi-step vegetation indices forecasting using multivariate time series," *Engineering Applications of Artificial Intelligence*, vol. 128, 2024.
- [17] R. Ahmad *et al.*, "A machine-learning based convlstm architecture for ndvi forecasting," *International Transactions in Operational Research*, vol. 30, no. 4, pp. 2025–2048, 2023.
- [18] S. Cavalli *et al.*, "A machine learning approach for ndvi forecasting based on sentinel-2 data." in *ICSOFIT*, 2021, pp. 473–480.
- [19] M. Beyer *et al.*, "Deep spatial-temporal graph modeling for efficient ndvi forecasting," *Smart Agricultural Technology*, vol. 4, p. 100172, 2023.
- [20] F. Zhao *et al.*, "Short and medium-term prediction of winter wheat ndvi based on the dtw-lstm combination method and modis time series data," *Remote Sensing*, vol. 13, no. 22, p. 4660, 2021.
- [21] A. Farbo *et al.*, "Forecasting corn NDVI through AI-based approaches using sentinel 2 image time series," *ISPRS Journal of Photogrammetry and Remote Sensing*, vol. 211, pp. 244–261, 2024.
- [22] V. Benson *et al.*, "Multi-modal learning for geospatial vegetation forecasting," in *Proceedings of the IEEE/CVF Conference on Computer Vision and Pattern Recognition*, 2024, pp. 27 788–27 799.
- [23] S. Zhao *et al.*, "VegeDiff: Latent diffusion model for geospatial vegetation forecasting," *IEEE Transactions on Geoscience and Remote Sensing*, 2025.
- [24] J. L. Hatfield *et al.*, "Temperature extremes: Effect on plant growth and development," *Weather and climate extremes*, vol. 10, no. Part A, 2015.
- [25] A. F. Ansari *et al.*, "Chronos-2: From univariate to universal forecasting," *arXiv preprint arXiv:2510.15821*, 2025.
- [26] M. Tortora *et al.*, "MATNet: Multi-Level Fusion Transformer-Based Model for Day-Ahead PV Generation Forecasting," *arXiv preprint arXiv:2306.10356*, 2023.
- [27] R. J. Hyndman *et al.*, "Automatic time series forecasting: the forecast package for r," *Journal of statistical software*, vol. 27, pp. 1–22, 2008.
- [28] S. Hochreiter *et al.*, "Long short-term memory," *Neural computation*, vol. 9, no. 8, pp. 1735–1780, 1997.
- [29] J. J. Hopfield, "Neural networks and physical systems with emergent collective computational abilities," *Proceedings of the national academy of sciences*, vol. 79, no. 8, pp. 2554–2558, 1982.
- [30] D. Salinas *et al.*, "DeepAR: Probabilistic forecasting with autoregressive recurrent networks," *International journal of forecasting*, vol. 36, no. 3, pp. 1181–1191, 2020.
- [31] H. Ismail Fawaz *et al.*, "InceptionTime: Finding alexnet for time series classification," *Data Mining and Knowledge Discovery*, vol. 34, no. 6, pp. 1936–1962, 2020.
- [32] Y. Nie, "A time series is worth 64 words: Long-term forecasting with transformers," *arXiv preprint arXiv:2211.14730*, 2022.
- [33] M. Jin *et al.*, "Time-LLM: Time series forecasting by reprogramming large language models," *arXiv preprint arXiv:2310.01728*, 2023.
- [34] I. Oguiza, "tsai - a state-of-the-art deep learning library for time series and sequential data," Github, 2023. [Online]. Available: <https://github.com/timeseriesAI/tsai>
- [35] O. Shchur *et al.*, "AutoGluon-TimeSeries: AutoML for probabilistic time series forecasting," in *International Conference on Automated Machine Learning*, 2023.
- [36] K. G. Olivares *et al.*, "NeuralForecast: User friendly state-of-the-art neural forecasting models." PyCon Salt Lake City, Utah, US 2022, 2022. [Online]. Available: <https://github.com/Nixtla/neuralforecast>
- [37] F. X. Diebold *et al.*, "Comparing predictive accuracy," *Journal of Business & economic statistics*, vol. 20, no. 1, pp. 134–144, 2002.